PHYSICAL REVIEW B **110**, 014430 (2024)

High magnetic field phase diagrams of the multiferroic manganite YMn_2O_5 single crystal

Haowen Wang,[*] Tian Li,[*] Yinfa Feng, Xinlong Shi, Chao Dong, Ming Yang,
Chengliang Lu, and Junfeng Wang[†]
*Wuhan National High Magnetic Field Center and School of Physics, Huazhong University of Science and Technology,
Wuhan 430074, China*

(Received 5 March 2024; accepted 2 July 2024; published 22 July 2024)

The magnetic field–temperature (H-T) phase diagram of the multiferroic manganite YMn_2O_5 has been investigated by magnetization and ferroelectric polarization experiments along the three crystallographic directions under the high magnetic field. For $H//a$, at 1.6 K, magnetization experiments reveal a significant anomaly in the magnetic field of 28 T, which is associated with a second-order phase transition into a fully polarized state characterized by the nearly saturated polarization (P) curve. Intriguingly, an additional first-order transition is observed at 10 T and 18 K and then gradually moves towards higher magnetic fields, and finally merges with the above transition with increasing temperatures. As a result, the two magnetic transitions lead to an exotic ν-like $P(H)$ curve, indicating the strong magnetoelectric coupling in YMn_2O_5. In particular, a field-induced P flip is realized at low temperatures, which may be attributed to the inversion of the vector spin chirality. Furthermore, this feature with distinct origins is also observed for other orientations of the magnetic field. In the $H//b$ geometry, a first-order spin-flop transition occurs below 18 K, compatible with the P reversal. However, no anomaly in magnetizations is found in the case of $H//c$. Note that the magnetization of YMn_2O_5 is far below its saturation value even up to 55 T. These studies could contribute to an in-depth understanding of the underlying physics in this family of compounds.

DOI: 10.1103/PhysRevB.110.014430

I. INTRODUCTION

Multiferroic materials, where magnetic and ferroelectric orders coexist and mutually couple, have recently received extensive attention in condensed-matter physics due to their intriguing properties and potential applications such as ultrasensitive sensors and information storage [1–6]. Among them, magnetic control of ferroelectricity is of significant interest because of the discovery of a giant magnetoelectric (ME) response in rare-earth manganese oxides [7–9]. The ferroelectricity in these materials is driven by the high degree of frustrated magnetic orders. It makes them rather sensitive to external perturbations including magnetic–electric fields [9,10], pressures [10–12], and chemical substitutions [13–15], since various magnetic states are close in energy and compete with the ground state. As a result, they demonstrate a large diversity of magnetic transitions related to distinct commensurate (CM) and incommensurate (ICM) magnetic modulations upon the change of temperatures, tuning the ferroelectric behaviors [8,16,17].

As a typical representative, the RMn_2O_5 (where R is a rare earth, Y, or Bi ion) manganites share nearly similar features with magnetic–ferroelectric phase transitions in spite of varying with the R ion [18–20]. Roughly speaking, below the Néel temperature T_N, incommensurate antiferromagnetic (AFM) orders are first established but still paraelectric (PE) phase. Subsequently, a lock-in transition occurs into a commensurate AFM ordering of Mn spins at T_{C1}, which is the onset of ferroelectric (FE) phases. Upon cooling, at T_{C2}, the magnetic system returns to incommensurate AFM orders again, accompanied by a rapid drop with the FE polarization. Besides, spin reorientations are identified in the CM phase of $DyMn_2O_5$ [21] and $HoMn_2O_5$ [22]. The above magnetic transitions are also shown in anomalies of the dielectric constant and thermal expansivity, indicating the strong spin-lattice coupling in these compounds. As expected, the pronounced change of ME effects can be observed by the application of hydrostatic pressure or magnetic field in these compounds [9,12,23]. The mechanism is mainly attributed to two magnetoelastic coupling modes [24,25]. One is the antisymmetric exchange Dzyaloshinskii-Moriya (or spin current) mechanism giving electric polarization proportional to a vector product of neighboring spins, i.e., $P_{SC} \propto [S_i \times S_j]$. The other is the symmetric exchange striction mechanism driven by Heisenberg exchange interaction proportional to a scalar product of neighboring spins, i.e., $P_{ES} \propto [S_i \cdot S_j]$. Nevertheless, it is a possibility that more than one mechanism is at work in a material system, e.g., coexistence of P_{SC} and P_{ES}, and which one is the dominant role based on the range of temperatures [26,27].

In the RMn_2O_5 family, YMn_2O_5 is of particular interest since its multiferroicity can be easily modified by external perturbations, leading to many appealing features [23,26–30]. Furthermore, the magnetic behavior of YMn_2O_5 is solely determined by the ordering of Mn^{3+} and Mn^{4+} ions at low temperatures due to a zero magnetic moment of Y^{3+}, suggesting no complex features caused by the magnetic interaction between the Mn and R ions. This also avoids the magnetic moment of Mn ions hiding in a large paramagnetic contribution

---

[*] These authors contributed equally to this work.

[†] Contact author: jfwang@hust.edu.cn

from R ions. As a consequence, it provides a fertile ground for studying the influence of chemical substitutions. For instance, the result from the Ga-substituted YMn_2O_5 indicates that the electric polarization is predominantly driven by the P_{ES} in the CM phase, while the P_{SC} is the main contribution to the electric polarization in ICM phase [26,27]. Magnetically, a ferrimagnetic phase is observed below a transition temperature of $T_N \sim 165$ K by substituting a part of Mn with Fe [29,31]. And, the magnetic moment can be significantly enhanced in Ca-doped YMn_2O_5 [32]. On the other hand, it has another advantage that YMn_2O_5 undergoes a ferroelectric polarization reversal upon the CM to low-temperature ICM transition [33]. Intriguingly, below T_{C2}, the polarization can be recovered at a critical pressure of 1 GPa and the ICM→CM transition is induced by pressures above 1.4 GPa [23,28,30]. Probably due to the abundant physical effects driven by the chemical doping and/or hydrostatic pressure in YMn_2O_5, previous studies mainly focus on altering the dopants or improving the value of pressures, but much less exploring the merit of magnetic fields. Indeed, magnetic fields may be more efficient to tune the multiferroic behavior of YMn_2O_5, since it can straightforwardly affect the magnetic moments. In addition, the isostructure of YMn_2O_5 has identified many intriguing phenomena resulting from magnetic fields. For example, the electric polarization can be magnetically flopped (90°) in $TmMn_2O_5$ [34] and $YbMn_2O_5$ [35], or magnetically reversed (180°) in $TbMn_2O_5$ [7]. Even a colossal magnetocapacitance is found in $DyMn_2O_5$ by application of a magnetic field [36]. It is worth mentioning that a topologically protected magnetoelectric switching was recently found in $GdMn_2O_5$ with the assistance of external magnetic field [1]. However, until now, there has been little research on the tunability of YMn_2O_5 by applying magnetic fields, especially utilizing the high magnetic field. Therefore, more experimental investigations on YMn_2O_5 need to be made by sweeping the magnetic field.

In this work, we report the evolution of multiferroic phase in YMn_2O_5 under the high magnetic field. Extensive characterizations, involving magnetic susceptibility, specific heat, low- (high-)field magnetization, and high-field ferroelectric polarization measurements, are performed detailedly. Based on the observed anomalies of magnetizations and polarizations, the magnetoelectric phase diagrams of the YMn_2O_5 single crystal are established along the three crystallographic axes, i.e., *a*-, *b*-, and *c*-axes. In particular, it is verified that the electric polarization can be reversed by the high magnetic field. This study gives a more comprehensive understanding for the fundamental physics in rare-earth multiferroic manganites RMn_2O_5.

II. EXPERIMENT

Single crystals of YMn_2O_5 were synthesized by the $PbO\text{-}PbF_2\text{-}B_2O_3$ flux method, as reported in earlier works [37]. Black plate-shaped crystals with a typical dimension of $2.5 \times 1.5 \times 1.5$ mm^3 were obtained after dissolving fluxes in dilute nitric acid. To check the phase purity, a few single crystals were ground into powder to be characterized by powder x-ray diffraction (XRD) at room temperatures. Then, Rietveld refinements of XRD data were performed by the GASA software package. As shown in Fig. 1(b), the powder XRD pattern displays a pure phase for these crystals. Furthermore, the difference between the experimental and Rietveld-profile refined data is very small, with a reliability factor $R_{wp} = 3.91\%$. Derived lattice parameters of YMn_2O_5 are $a = 7.2678$ Å, $b = 8.4815$ Å, and $c = 5.6692$ Å, which are in good agreement with earlier studies [26,38]. In addition, the phase and single crystallinity were also checked by the slow-scan XRD pattern onto the natural growth plane. As a typical sample, Fig. 1(c) clearly demonstrates quite sharp diffraction peaks indexed by the (0*k*0) reflections of YMn_2O_5, evidencing the good quality of the crystals. The crystallographic orientation was determined using the x-ray Laue diffraction, and then it was mechanically cut into thin rectangles with a wide *ac* plane. Before the high magnetic field experiments, both magnetization- (M) and specific-heat (C) dependent temperatures and/or magnetic fields, had been

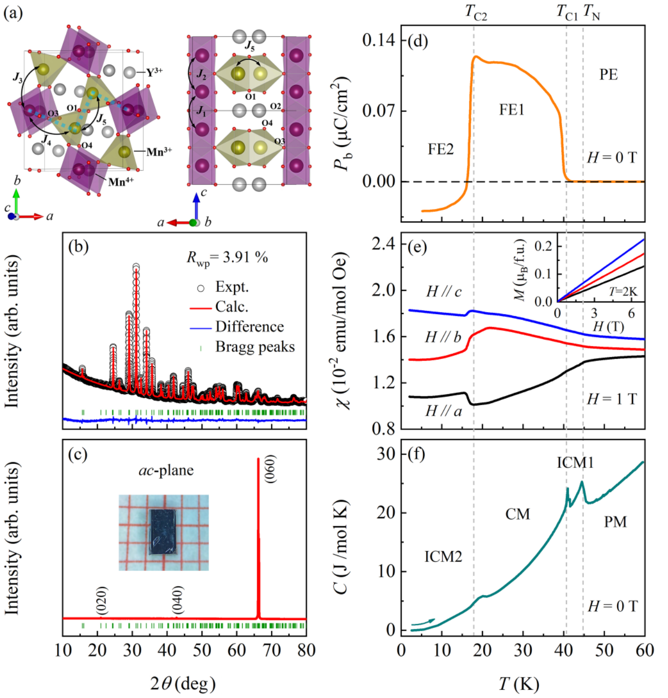

FIG. 1. (a) Crystal structure of YMn_2O_5 projected in the *ab* plane (left panel) and *ac* plane (right panel). The black rectangle denotes the unit cell. Dotted cyan lines indicate the zigzag chains along the *a* axis. Also shown are the magnetic exchange interactions $J_1 - J_5$ [38,49]. J_1 and J_2 represent the exchange interaction between neighboring Mn^{4+} spins through the Y^{3+} layer and Mn^{3+} layer along the *c* axis, respectively. J_3 and J_4 represent the interchain- and intrachain-exchange interactions between Mn^{3+}-Mn^{4+} spin pairs, respectively. J_5 represents the exchange interaction between neighboring Mn^{3+} spins in the bipyramid. (b) Rietveld refinement of the powder XRD pattern for YMn_2O_5. (c) X-ray diffraction pattern of (0*k*0) plane for YMn_2O_5. The inset shows a photograph of the representative single-crystal YMn_2O_5. (d) Temperature dependence of the electric polarization at $H = 0$ adopted from Ref. [28]. (e) Temperature dependence of the magnetic susceptibility χ along *a*, *b*, and *c*, respectively. The inset shows the corresponding magnetization as a function of H at $T = 2$ K measured using SQUID. (f) Temperature dependence of the specific heat at $H = 0$.

characterized by the commercial superconducting quantum interference device (SQUID) and physical property measurement system.

High-field magnetization and electric polarization measurements were conducted in the Wuhan National High Magnetic Field Center using a 10.5-ms short-pulse wave generated by a nondestructive magnet. The high-field $M(H)$ curves at various temperatures were measured by the standard induction method employing a coaxial pickup coil and calibrated by a comparison with the low-field data. The high-field $P(H)$ data at various temperatures were gained by means of the pyroelectric technique. In detail, gold electrodes were sputtered onto the opposite faces perpendicular to the b axis so that all electric polarizations were performed along this direction (P_b). The sample was first cooled from far above the Néel temperature down to target temperatures with applying electric field (E) under zero magnetic field. Subsequently, a pyroelectric current (I) as a function of H was detected by measuring the voltage variation across a shunt resistor R_s during the short pulse. The $P(H)$ curve was derived from integrating the pyroelectric current with the time. It is worth mentioning that a bias electric field of $E = 6$ kV/cm was used before and preserved during each pulse to fully polarize ferroelectric domains in samples.

III. RESULTS

The orthorhombic structure of YMn_2O_5 belongs to the *Pbam* (No. 55) space group at room temperature [33]. The left panel of Fig. 1(a) displays the crystallographic unit cell, which is composed of 4 Y ions and 8 Mn ions. According to occupying distinct Wyckoff sites, Mn ions are divided into two groups, i.e., Mn^{4+} ($4f$) and Mn^{3+} ($4h$). Mn^{4+} ($S = 3/2$) is coordinated with 6 oxygen ions forming a distorted octahedron, while Mn^{3+} ($S = 2$) is coordinated with 5 oxygen ions forming a square pyramid. The $Mn^{4+}O_6$ octahedra share common edges with the neighbors to form a chain along the c axis, and a pair of $Mn^{3+}O_5$ pyramids connect these chains as a bridge [see the right panel of Fig. 1(a)]. As a consequence, in the ab plane, zigzag chains of $Mn^{4+}O_6$ octahedra and $Mn^{3+}O_4$ square pyramids stretch along the a axis, and are stacked along the b axis. A rare-earth ion Y^{3+} is embraced by the pentagonal network of Mn^{4+} and Mn^{3+} ions generating a double-capped trigonal prism. Here, Mn^{3+} and Y^{3+} ions come into being an alternative layer between adjacent Mn^{4+} layers in the c direction.

Frustrated spin-exchange interactions are an intrinsic behavior in the spin system of YMn_2O_5, which stem from a geometrical ring consisted by five Mn spins (Mn^{4+}-Mn^{3+}-Mn^{3+}-Mn^{4+}-Mn^{3+}) in the ab plane [19,33,39]. This restricts all nearest-neighbor spins being antiparallel in the ring and leads to a noncollinear magnetic structure. Hence, upon cooling, YMn_2O_5 undergoes a series of successive transitions due to the complex crystal structure and magnetic frustration [18,40]. At $T_N \sim 45$ K, the moments of Mn^{4+} and Mn^{3+} ions develop a two-dimensionally modulated incommensurate magnetic ordering (2DICM) with $\mathbf{q_M} = (q_x, 0, q_z)$, which is followed by one-dimensionally modulated incommensurate magnetic orderings (1DICM) with $\mathbf{q_M} = (q_x \sim 0.492, 0, 0.25)$ around $T_{C1} \sim 40$ K. Concurrently, a weak spontaneous electric polarization (WFE) appears along the b axis. For convenience, both 2DICM and 1DICM are referred to as the ICM1 phase in this study. Slightly below T_{C1}, a commensurate magnetic structure with $\mathbf{q_M} = (0.5, 0, 0.25)$ occurs simultaneously with a remarkable ferroelectric phase (FE1). Upon further cooling to $T_{C2} \sim 18$ K, the magnetic structure with $\mathbf{q_M} = (0.48, 0, 0.292)$ becomes incommensurate again (ICM2) and another suppressed ferroelectric phase (FE2) is observed, where P is reversed from the $+b$ to $-b$ direction [see Fig. 1(d)].

The temperature dependence of the magnetic susceptibility χ along three crystalline axes at $H = 1$ T is shown in Fig. 1(e). At first, a typically magnetic anisotropy ($\chi_c > \chi_b > \chi_a$) can be is clearly identified at the entire temperature range. Between T_N and T_{C2}, the susceptibility χ_a gradually decreases with an opposite behavior for χ_b and χ_c. An abrupt variation takes place around T_{C2}, namely, the χ_a enhances significantly while both χ_b and χ_c show an obvious reduction, corresponding to the flip of polarizations. Upon further cooling, a subtle change of three susceptibilities is determined. Note that there is no identifiable anomaly in $\chi(T)$ curves at T_{C1}, but a sharp peak is easily found in the $C(T)$ curve [see Fig. 1(f)]. In addition, a strong peak and broad bump are also observed at T_N and T_{C2}, respectively. As a result, the ground state ($H = 0$) of YMn_2O_5 is roughly divided into four regions including PM/PE, ICM1/PE (WFE), CM/FE1, and ICM2/FE2.

To get more details of the evolution with ground state of YMn_2O_5, $M(H)$ measurements have been carried out at various temperatures using the SQUID magnetometer. Unexpectedly, the profile of the $M(H)$ curve behaves as a strictly linear increase up to 7 T for all orientations, which is the type characteristic of antiferromagnetic coupling between magnetic ions, as a typical example shown in the inset of Fig. 1(e). However, the ground state in its isostructure RMn_2O_5, can be easily modified by the application of magnetic fields. There have been exhibited, for example, $GdMn_2O_5$ ($\sim$4.7 T) [9], $ErMn_2O_5$ ($\sim$1.5 T) [41], $DyMn_2O_5$ ($\sim$2 T) [42], and so on. This observation in YMn_2O_5 is reminiscent of the magnetic properties of the compound $BiMn_2O_5$ for a comparison [43]. As a similarity, both Bi^{3+} and Y^{3+} are nonmagnetic at A sites and magnetic exchange interactions mainly derive from Mn^{3+} and Mn^{4+}. In $BiMn_2O_5$, application of high magnetic fields ($\sim$18 T) along the a axis reveals a Mn spin-flop transition with a concomitant change of P polarities. Hence, the study for YMn_2O_5 under the high magnetic field is rather desirable and fascinating.

Generally, high magnetic fields provide a good opportunity to explore unknown phase transitions and intriguing multiferroic properties. For example, we found a flexible control of quantum magnetization plateau and high-field ferroelectricity in $Ni_2V_2O_7$ [44] and a colossal linear magnetoelectricity in $Fe_2Mo_3O_8$ by pulsed high fields recently [2]. For YMn_2O_5, we now focus on the magnetization dependent with magnetic fields extending the measurement up to the high field at various temperatures. Measurements are repeated several times to ensure the reproducibility of the data. Figure 2(a) exhibits a few typical magnetization curves with magnetic fields along the a axis. At 1.6 K, the $M(H)$ curve possesses a completely linear behavior below $\sim$20 T. Then, the curve increases quickly until $\sim$26 T, followed by a steplike anomaly.

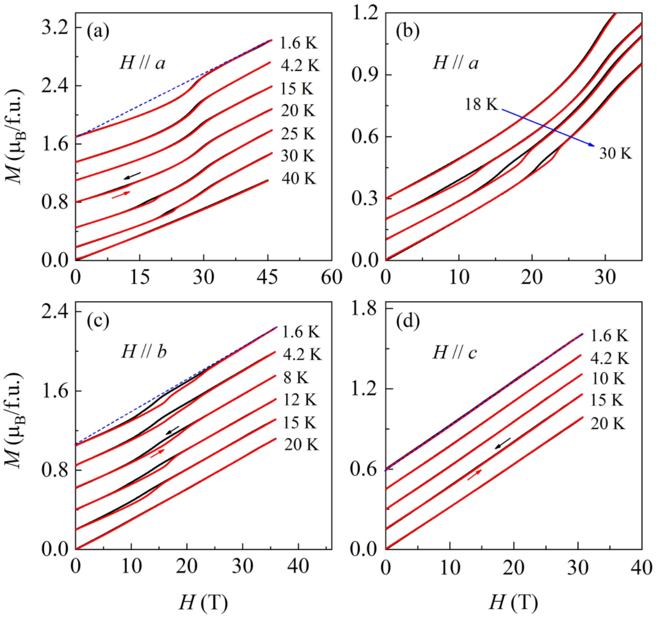

FIG. 2. Measured high-field magnetization as a function of H at various temperatures along different crystallographic axes: (a) $H//a$; (c) $H//b$; and (d) $H//c$. The blue dashed lines exhibit linear extrapolation of the magnetization data to zero fields. (b) The amplified $M(H)$ curve for $H//a$ in the range of 18–30 K. The red (black) curve denotes the field-rising (-falling) sweep. Data are shifted vertically for clarity.

The anomaly might be attributed to the spin-flop transition of the Mn ions form AFM zigzag spin chains. Further increasing the magnetic field, the magnetization increases linearly with H up to 55 T again (see Fig. S1 of the Supplemental Material [45]). It is possible that the magnetic moments of Mn ions are tilted towards H slowly after the spin-flop transition, resulting in a continuous enhancement with magnetizations in the high-field region. With regard to the verification of the spin-flop transition, there are two reasons for this. One is the small value of the magnetization; e.g., the intensity of M is stabilized at 0.8 μ_B/f.u. around 30 T, which is far less than the saturation value of both Mn^{3+} and Mn^{4+} ions. The other is a zero crossing of the linearly extrapolated line (see blue dashed line), suggesting the survival of the AFM interaction beyond 30 T. This scenario is reminiscent of magnetic characteristics in the isostructure $BiMn_2O_5$ that a spin-flop transition is found at ∼18 T by the application of magnetic field along the a axis [43]. Such discrepancy of the critical field may be attributed to the different ion radius between Y^{3+} (1.019 Å) and Bi^{3+} (1.17 Å) resulting in the distinct exchange interaction and magnetic anisotropy [47]. Previous studies have established that the arrangement of Mn spins within the ab plane is largely dominated by the J_3, J_4, and J_5 exchange interactions [see the left panel of Fig. 1(a)] [20,38,43,48,49]. Moreover, these exchange interactions are closely associated with the bond length Mn–Mn and bond angle Mn–O–Mn. Compared with $BiMn_2O_5$, the bond length Mn^{3+}-Mn^{4+} of YMn_2O_5 associated with the J_3 and J_4 interactions significantly decreases while the variation of the bond angle Mn^{4+}-O4/O3-Mn^{3+} is rather weak, enhancing the strength of exchange interactions (see Table S1 of the Supplemental Material [45]). For J_5, the effect stemming from the shrinkage of bond angle Mn^{3+}-O1-Mn^{3+} may be overshadowed by the pronounced decease in the bond length Mn^{3+}-Mn^{3+}, possibly strengthening the AFM interaction. As a result, for YMn_2O_5, a higher magnetic field is needed to gain more Zeeman energy to drive the spin-flop transition. In addition, Jeon *et al.* proposed a theoretical model to describe the critical field H_c on the spin-flop process in $BiMn_2O_5$, i.e., $H_c = \sqrt{J}I$, where J and I are, respectively, the exchange and local anisotropy energies [48]. Although the determination of I is quite hard in the present work, we note that the bond distance Mn^{3+}-O3(2.015 Å) of YMn_2O_5 is far less than that of $BiMn_2O_5$ (2.085 Å) compared with others [45], probably leading to a large single-ion anisotropy in the pyramid. Further investigations assisted by the theoretical calculation are necessary to resolve this issue. With increasing temperature, the anomaly slowly moves to higher fields. For instance, it is enhanced by approximately ∼2.5 T as the temperature is up to 30 K. Interestingly, above 18 K, an additional anomaly is seen at a lower field and increases drastically with increasing T, such as, it rises from ∼10 T at $T = 18$ K to ∼23 T at $T = 30$ K. Note that the anomaly in the low-field region displays a magnetic hysteresis while this in the high-field region does not show a distinct loop, indicating the different origins between them [see Fig. 2(b)].

For magnetic fields along the b direction, the behavior of magnetizations is roughly similar to the data for $H//a$ at low temperatures. Figure 2(c) demonstrates the magnetization processes of $YMnO_3$ in magnetic fields up to 36 T. At 1.6 K, M increases linearly with H up to 12 T. Then, a broad steplike transition shows a large magnetization jump $\Delta M \sim 0.5\ \mu_B$. If taking a closer look at this range of the $M(H)$ curve (12 T < H < 25 T), three successive steplike anomalies can be identified around 16.5, 22, and 23 T, respectively. In higher magnetic fields up to 51 T (see Fig. S1 of the Supplemental Material [45]), this feature is given by a linear increase which can be extrapolated to zero fields with a blue dashed line, similar to the behavior of $H//a$. Differently, the hysteresis loop is found at these anomalies, indicating that the anomaly is a first-order phase transition. As the temperature increases, these anomalies demonstrate an opposite trend with $H//a$; i.e., they gradually merge and shift to the low magnetic field as T is increased. Furthermore, the hysteresis is also preserved up to 18 K. Even more astonishing, unlike $H//a$, no transition is visible and the curve of $M(H)$ increases linearly above 18 K [see Fig. 2(c)]. In the case of $H//c$, as exhibited in Fig. 2(d), there is no anomaly in $M(H)$ curves for H up to 31 T at 1.6 K, and the linear behavior can be kept up to 54 T (see Fig. S1 of the Supplemental Material [45]). Namely, the magnetization does not show any sign of saturation even at the highest magnetic field, indicating the robustness of the AFM structure in YMn_2O_5. Moreover, with increasing temperature, the typically linear behavior is retained all the time and no anomaly is discovered even surpassing 18 K. However, three crystallographic axes of $M(H)$ curves all present the spin-flop transition in $GdMn_2O_5$ at low temperatures, which corroborates the effect of Mn-R exchange interactions [50,51].

Due to the ultrafast sweeping rate of the pulsed field (dH/dt), a slight variation of P can still be detected by the pyrocurrent technique, which actually records the voltage

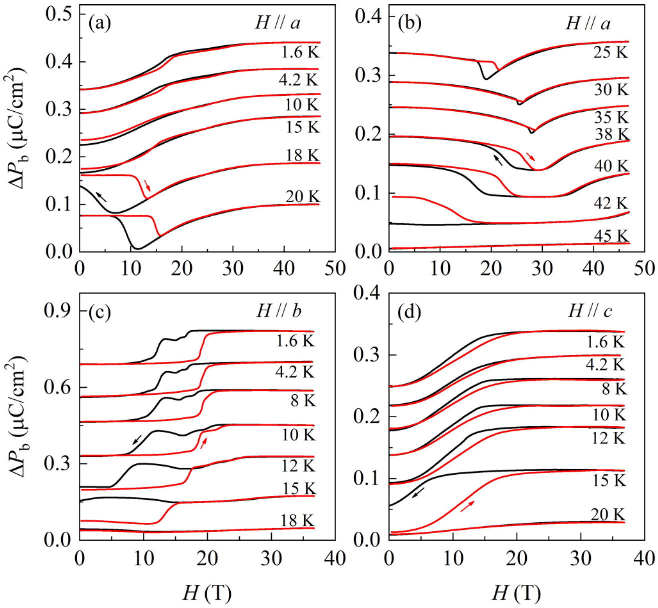

FIG. 3. ΔP_b as a function of H measured at various temperatures under the high magnetic field. (a), (b) $H//a$; (c) $H//b$; and (d) $H//c$. The red (black) arrows denote the field-rising (-falling) sweeps. For clarity, the curves have been moved vertically.

variation passing a shunt resistor. In consequence, we investigate the P change of YMn_2O_5 in pulsed magnetic fields along the three crystallographic axes. Reproducibility of the data is determined by means of repeating measurements for each orientation. Figures 3(a) and 3(b) show the data of YMn_2O_5 with the magnetic field applied parallel to the a axis at various temperatures, where the variation of P is defined as $\Delta P_b = P_b(H) - P_b(H = 0)$. At 1.6 K, P monotonously increases about 0.04 $\mu C/cm^2$ in magnitude before $H \sim 15$ T. In quick succession, the characteristic feature of $P(H)$ curves is given by the successive steplike anomalies. The low-field anomaly with a small hysteresis can be clearly observed around $H_{c1} \sim 17$ T. If taking a closer look at the trace of polarizations, the high-field anomaly is also recognized around $H_{c2} \sim 28$ T. In higher magnetic fields up to 35 T, the value of polarizations is about 0.1 $\mu C/cm^2$ with going to saturation. Decreasing the magnetic field from 47 T, the P goes back to the original position. With the increase of temperature up to 18 K, a complete change has taken place in the profile of $P(H)$. At low magnetic fields below 9 T, the value of P remains unchanged in the H-increasing sweep. And then, a large ν-like curve is identified at the intermediate-H region (10 T $< H <$ 23 T). In addition, the minimal value of ΔP_b reaches -0.05 $\mu C/cm^2$ at $H_{min} \sim$ 13.3 T and then a subtle anomaly is observed out of the ν-like curve. As H is further increased, the polarization nearly saturates above the critical magnetic field of 37 T. Interestingly, with decreasing the H back to zero, P does not recover the initial value at $H = 0$, but displays a residual polarization of about -0.023 $\mu C/cm^2$ accompanied by a large hysteresis loop below H_{min}. When the temperature is increased, the residual polarization vanishes above 20 K. Meanwhile, the hysteresis loop gradually shrinks and nearly disappears above 30 K. Unexpectedly, a large ν-like $P(H)$ curve starts to emerge at T = 38 K, i.e., a polarization plateau. The minimal value of ΔP_b is located at $H \sim 29$ T in the H-increasing process. Besides, a large hysteresis loop reappears in the intermediate-H region (18 T $< H <$ 28 T) and no residual polarization is visible. With increasing T, the width of the polarization plateau ΔH becomes broader and the hysteresis loop gradually shifts to lower magnetic fields. As a result, a large residual polarization of about -0.046 $\mu C/cm^2$ is clearly observed at $T = 42$ K. Further increasing the temperature, the $\Delta P_b(H)$ curve turns into a smooth straight line and no anomaly is found above 45 K.

The polarization behavior of YMn_2O_5 for $H//b$ is shown in Fig. 3(c) in pulsed magnetic fields up to 37 T. In comparison with $H//a$, several distinct features from the $\Delta P_b(H)$ curve are clearly recognized: (1) A hysteresis of the H-induced ferroelectricity becomes larger below 20 T. As the temperature increases, it gradually moves towards the lower field, leading to a big remanent polarization of about 0.08 $\mu C/cm^2$ at $T = 15$ K; (2) several successive anomalies are clearly seen in the falling sweep (the black curve) while it is invisible in the rising sweep (the red curve). Furthermore, they depend on the sample, evidenced by $\Delta P_b(H)$ curves of sample No. 2 (see Fig. S2 of the Supplemental Material [45]). This is interpreted as magnetoelectric domains, and a similar phenomenon is also found in the $GdMn_2O_5$ [9]; and (3) when the temperature is higher than 18 K, no anomaly can be discovered in the entire range of magnetic fields. For H along the c axis, the measured $\Delta P_b(H)$ curves at several typical T's are shown in Fig. 3(d). It is evident that at 1.6 K a broad steplike anomaly with a hysteresis emerges below 20 T. With a further increase of the magnetic field, ΔP_b enters a flat region. However, in contrast to the $\Delta P_b(H)$ curve, the $M(H)$ curve for $H//c$ does not exhibit any anomaly over the entire field range. This observation is reminiscent of the multiferroic property of $PrMn_2O_5$, in which an electric polarization occurs above ~12 T along the b axis while no anomaly is observed in the $M(H)$ curve [52]. It is attributed to magnetically driven ferroelectricity originating from the coupling between Mn^{3+} and Pr^{3+} ions rather than Mn^{3+} and Mn^{4+} ions. Notably, this explanation does not fit the present case of YMn_2O_5. Furthermore, it is impossible that the imperfect alignment of the c axis and H gives rise to this anomaly, since the change of polarizations can be as large as 0.09 $\mu C/cm^2$ at $H \sim 22$ T approximating to the value in the cases of $H//a$ or $H//b$. Upon warming, the profile of the $\Delta P_b(H)$ curve is nearly independent with the temperature below 12 K. As temperature is increased to 15 K, a remanent polarization about 0.043 $\mu C/cm^2$ and large hysteresis are clearly seen, which may derive from the motion of domains. Alternatively, P monotonously increases up to 0.02 $\mu C/cm^2$ at $H \sim 37$ T and 20 K, displaying a completely different response to the H compared with the case in the ab plane. Consequently, a dramatic ME anisotropy is found in YMn_2O_5 by the pulsed magnetic field.

Generally, the magnetic and ferroelectric orders of RMn_2O_5 have a strong coupling effect [41–43,50,51]. It will no doubt motivate us to further understanding the relationship between M and P in YMn_2O_5. The derivative dM/dH and dP_b/dH as a function of H in various temperatures are shown in Fig. 4. For clarity, only the data from the rising field sweeps are applied. For H along the a axis, the symmetric peak (pink arrows) in dM/dH curves [Fig. 4(a)] is

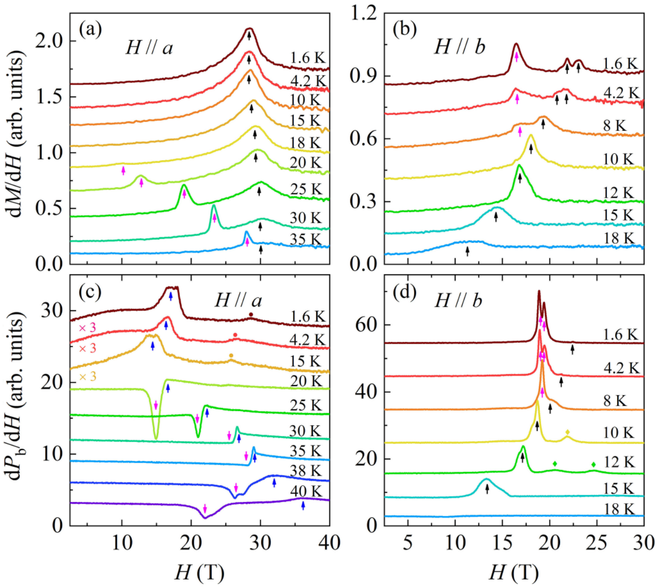

FIG. 4. The derivative dM/dH as a function of H measured at various temperatures for (a) $H//a$; (b) $H//b$. The derivative dP_b/dH as a function of H measured at various temperatures for (c) $H//a$; (d) $H//b$. For clarity, only the data from the rising field sweeps are shown. Data are vertically offset.

accompanied by a corresponding anomaly (pink arrows) in dP_b/dH curves [Fig. 4(c)]. And, the very weak bump (closed circles) in dP_b/dH curves corresponds to the high-field peaks (black arrows) in dM/dH curves. However, not any sign of dM/dH curves corresponds to these peaks (blue arrows) in the dP_b/dH curves. For H along the b axis, these anomalies (black and pink arrows) in the dM/dH curve [Fig. 4(b)] gradually move close and merge together below 10 K. As the temperature further rises, the resultant peak moves to the low magnetic field. Correspondingly, the evolution of anomalies in the dP_b/dH curves [Fig. 4(d)] more or less coincides with these anomalies presented in the dM/dH curves. Besides, some satellite peaks (yellow and green diamonds) are observed in the dP_b/dH curve from 10 to 12 K but disappear above 15 K. We anticipate that these satellites may be the signature from the domains. Hence, the inherent coupling between the magnetism and ferroelectricity is determined in YMn_2O_5.

Derived from the peak positions of the $M(H)$ and $P(H)$ curves with the field-rising sweep, we construct the magnetic field–temperature (H-T) phase diagrams of YMn_2O_5 for external magnetic fields along the a, b, and c axes and show the results in Figs. 5(a), 5(b), and 5(c), respectively. In the case of $H//a$, three phase boundaries are defined by T_N, T_{C1}, and T_{C2} at the ground state (see Fig. 1) and low-field region ($H < 15$ T). These phase boundaries coincide with the phase transitions PM/PE → ICM1/PE (WFE) at T_N, ICM1/PE (WFE) → CM/FE1 at T_{C1}, and CM/FE1 → ICM2/FE2 at T_{C2}. For the intermediate-H region (15 T $< H <$ 25 T), the phases FE1 and FE2 smoothly transform to the FE3 phase below 35 K. As the magnetic field is further increased, a pink dashed line is clearly identified round 28 T and insensitive to the temperature in the FE3 phase, which represents the spin-flop transition of Mn ions. However, at the higher temperature, the ICM1/PE (WFE) phase can be preserved in the high-H region regardless of its areas. The phase diagram for $H//b$ shows a comparable phase sequence as observed for $H//a$ in the low-field region ($H < 15$ T). With increasing fields, the ICM2/FE2 phase is completely replaced by the CM/FE1 phase, except for a coexistence region of FE1 and FE2 phases below 10 K, as shown in Fig. 5(b). For $H//c$, it can be directly observed that no fresh phase is induced by the high magnetic field [see Fig. 5(c)]. Furthermore, there is a clear boundary between FE1 and FE2 above 15 K from the $\chi(T)$ curves, as presented in Fig. S3(c) of the Supplemental Material [45]. It is worth mentioning that the phase diagram of $GdMn_2O_5$ shares a common feature for the H along three crystallographic axes [50]. Nevertheless, the significant anisotropy with ME phase diagrams occurs unexpectedly in YMn_2O_5.

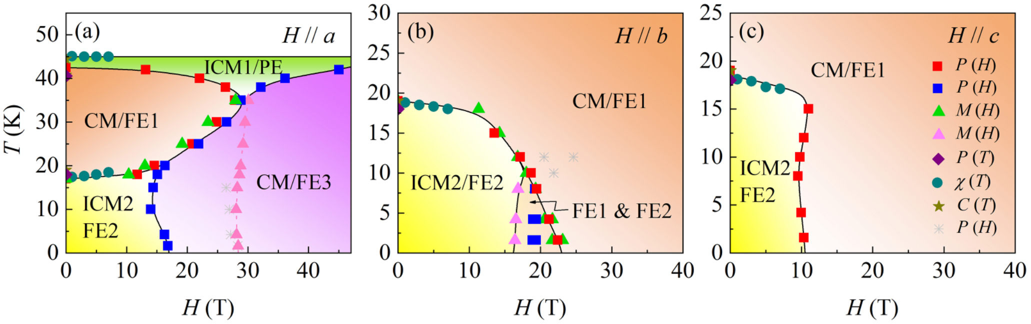

FIG. 5. High-field ME phase diagrams of YMn_2O_5 derived from the data for increasing fields along different crystallographic axes: (a) $H//a$; (b) $H//b$; and (c) $H//c$. Closed squares and asterisks denote the data obtained from $P(H)$ curves. Closed triangles and closed circles denote the data obtained from $M(H)$ and $\chi(T)$ curves, respectively. Closed stars and diamonds denote the data obtained from $C(T)$ and $P(T)$ [28], respectively. The abbreviations in the drawing represent the following: ICM1 = high-temperature incommensurate magnetic phase, ICM2 = low-temperature incommensurate magnetic phase, CM = commensurate magnetic phase, PE = paraelectric phase, FE1 = ferroelectric phase 1, FE2 = ferroelectric phase 2, FE3 = ferroelectric phase 3, and FE1 and FE2 = the coexistence of FE1 and FE2. The solid lines are guides for eyes. The pink dashed line in phase CM/FE3 shows the spin-flop transition.

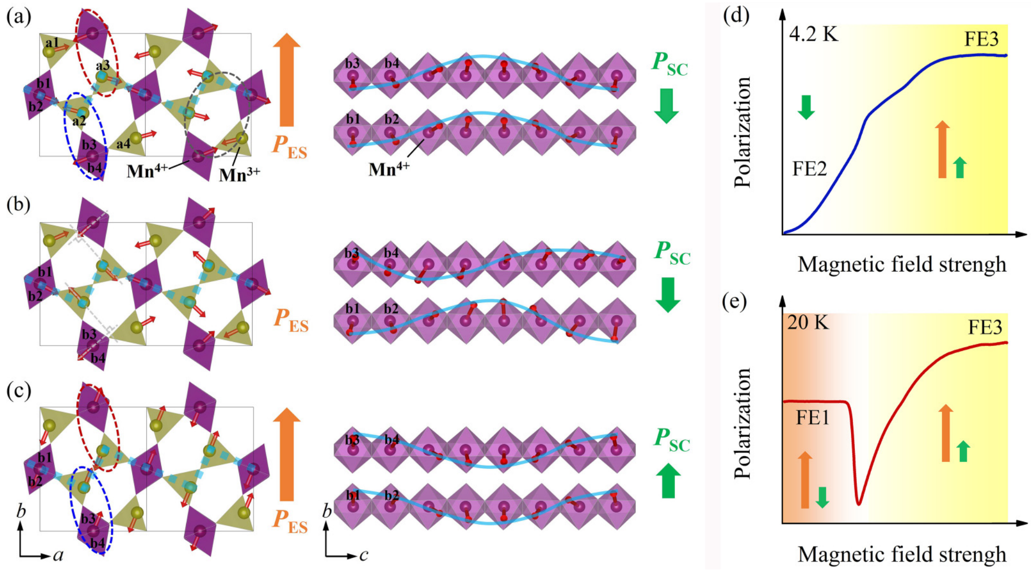

FIG. 6. Crystal and magnetic structures of YMn_2O_5 projected in the *ab* plane (left panel) and *bc* plane (right panel) for (a) CM/FE1 [19,33], (b) ICM2/ FE2 [19,33], and (c) CM/FE3. The dark yellow (purple) spheres denote Mn^{3+} (Mn^{4+}) ions, and corresponding Mn-O polyhedra are displayed with the same color. Dotted cyan lines denote the antiferromagnetic chains along the *a* axis. Thin red arrows denote the Mn spin moments. The unit cell is shown by the black rectangle. The gray dashed ellipse denotes a ring consisting of five Mn spins (Mn^{4+}-Mn^{3+}-Mn^{3+}-Mn^{4+}-Mn^{3+}). Thick orange (green) arrows denote electric polarizations induced by the symmetric exchange striction (spin-current) mechanism in *ab* (*bc*) plane. The red (blue) dashed ellipse indicates attractive and repulsive interactions between Mn^{3+} and Mn^{4+} ions. The cyan curves denote spirals formed by the Mn^{4+} ions. As an exemplification, the evolution process of *P* with increasing magnetic field of *H*//*a* is illustrated at (d) 4.2 K and (e) 20 K.

IV. DISCUSSION

The above experimental results have clearly demonstrated complex ME phase diagrams of YMn_2O_5 under the high magnetic field. In particular, a dramatic ME anisotropy is driven by the magnetic field along three crystallographic orientations. In the following, we will attempt to discuss the possible origin of the observed ME responses in each phase. Utilizing the single-crystal neutron diffraction, the magnetic structures of YMn_2O_5 at $H = 0$ were given by Kim and Vecchini *et al.* [19,33]. Consequently, the ferroelectricity of YMn_2O_5 can be well interpreted relying on the magnetoelastic coupling models [24,25]. In the CM/FE1 phase, to release the frustration in a ring consisting of five Mn spins (gray dashed ellipses), Mn^{3+} spins antiparallel to the Mn^{4+} (red dashed ellipses) move closer to each other, while Mn^{3+} spins with parallel configuration (blue dashed ellipses) move away from each other. As a result, the magnetostriction mechanism leads to a ferroelectric polarization $P_{ES}//+b$ (large orange arrows) in the *ab* plane [left panel of Fig. 6(a)]. On the other hand, the *bc* components of Mn^{4+} spins form a cycloidal spiral along the *c* axis, which gives rise to a ferroelectric polarization $P_{SC}//-b$ (large green arrows) based on the spin-current mechanism [right panel of Fig. 6(a)]. Hence, the total electric polarization (P_{tot}) of FE1 is constituted of two different components, i.e., $P_{tot} = P_{ES} - P_{SC}$. Since the P_{ES} is dominant in the CM/FE1 phase, the electric polarization in FE1 has a positive sign, as shown in Fig. 6(e). For the ICM/FE2 phase, the P_{ES} is quite weak or even lost because the Mn^{3+}-Mn^{4+} spin pairs along the *b* axis (gray dashed lines) are almost orthogonal. Nevertheless, the P_{SC} is well preserved by the ICM modulation period. Accordingly, the ferroelectricity is predominantly driven by the P_{SC} in the ICM2/FE2 phase, as shown in Figs. 6(b) and 6(d).

It is worth noting that the typical value of P_{tot} at $H = 0$ is as small as approximately -0.03 μC/cm^2 in the FE2 phase, which is obtained from the $P(T)$ curve in earlier works [27,28]. For our results, the intensity of $\Delta P_b[= P_b(H_{c1}) - P_b(H = 0)]$ is just right around this value at low temperatures. Namely, a polarization reversal is extremely likely to take place at the phase boundary between the FE2 and FE3 phases when *H* is applied along the *a* axis [see Fig. 6(d)]. A similar phenomenon is also found in our previous papers that the direction of polarization in the low-field ferroelectric phase (AF2) is completely opposite to the high-field ferroelectric phase (*IV*) in multiferroic $MnWO_4$ [53]. Generally, the orientation of *P* is decided by the vector spin chirality $C(= S_i \times S_j)$ in the spiral spin system. In other words, magnetic control of the *C* orientation can realize the *P* reversal. In present case, this means that the *C* of Mn^{4+} spins should be changed from one direction along the *a* axis to the other at the FE2/FE3 transition, as shown in the right panels of Figs. 6(b) and 6(c). The sign reversal of the electric polarization can also be induced by the hydrostatic pressure in YMn_2O_5, accompanied by the phase transition from the ICM2 to the CM phase [28]. Here, the detail value of $\mathbf{q_M}$ in FE3 cannot been determined due to the lack of neutron-diffraction measurements, but we can deduce it belongs to the CM phase from our data. There are two reasons as follows: First, at 1.6 K, the change of polarizations $[\Delta P_b = P_b(H) - P_b(H = 0)]$ is up to 0.1 μC/cm^2 at high magnetic fields, approximating the value in the scenarios of *H*//*b* and *H*//*c*. It is not possible that the pronounced increase of polarizations merely stems from the inversion of P_{SC} (~ -0.03 μC/cm^2) from negative to positive. And, the

P_{ES} from the magnetostriction mechanism is essential for the change of polarizations ΔP_{b}. As is well known, the magnetostriction mechanism needs the commensurate spin order and low symmetry on the specific chemical lattice. Hence, the FE3 is a modulated commensurate magnetic phase. In addition, we note that the magnetic field–temperature (H-T) and pressure–temperature (P-T) phase diagrams of the isostructure $\mathrm{HoMn_2O_5}$ are very similar to one another, or are nearly identical as the magnetic and pressure axes are normalized [54,55]. For $\mathrm{YMn_2O_5}$, Kozlenko *et al.* emphasized that the application of hydrostatic pressure ($P > 1$ GPa) can gradually suppress the low-temperature ICM phase and CM phase with $\mathbf{q_M} = (0.5, 0, 0.25)$ and induce the appearance of the CM phase with $\mathbf{q_M} = (0.5, 0, 0.5)$ [23,30]. Following this way, the FE3 should be located in the CM phase [see Fig. 5(a)], but its propagation vector $\mathbf{q_M}$ still remains unclear and needs to be further investigated by neutron-diffraction techniques. Indeed, the analogy-based method has been successfully applied in $\mathrm{YMn_2O_5}$, such as the discovery of the one-dimensionally modulated incommensurate magnetic ordering (1DICM) with $\mathbf{q_M} = (q_x \sim 0.492, 0, 0.25)$ compared with $\mathrm{ErMn_2O_5}$ [40,56].

When the system reaches the FE3 phase, the P_{ES} is activated and works together with the P_{SC}, resulting in the continuous increase of P_{tot}. As the magnetic field further increases, P_{SC} and P_{ES} rotate to the same direction, leading to the saturation of P_{tot} in $\mathrm{YMn_2O_5}$ [see Fig. 6(c)]. Note that the boundary between FE1 and FE3 phases corresponds to a first-order magnetic phase transition while no magnetic anomaly is found at the FE2/FE3 phase boundary [see Fig. 5(a)]. Perhaps only the former invokes the spin reorientation of Mn ions in the *ab* plane, which gives rise to the sharp drop of P_{tot} at the FE1/FE3 boundary leading to a large ν-like $P(H)$ curve, as presented in Fig. 6(e). We recall that similar features are also found in $\mathrm{GdMn_2O_5}$ in magnetic field-dependent experiments, i.e., the P decrease occurs around the first-order magnetic phase transition, which is attributed to the asynchronized motion among two inequivalent Mn chains [1,9]. We consider that the anomaly at the FE1/FE3 boundary originates from the same reason. It is noteworthy that the second-order spin-flop transition of Mn ions (pink dashed line) in the FE3 phase does not induce a new ferroelectric phase, but could affect slightly polarization value leading to the weak bump [gray asterisks in Fig. 5(a)] in dP_{b}/dH curves [see Fig. 4(c)]. Indeed, this case is not rare and has been found in $\mathrm{Co_2V_2O_7}$ [57]. Although the second-order transition likewise occurs in $\mathrm{YMn_2O_5}$, the relative orientation of neighboring Mn spins could be different from the case of $\mathrm{BiMn_2O_5}$ [43]. According to the comparative analysis of magnetic structures between them [19], several factors should be of concern despite no conclusive answer. First, the angular deviation of staggered Mn moments from the *a* axis (θ) is more pronounced in $\mathrm{YMn_2O_5}$. Furthermore, the θ angle of $\mathrm{YMn_2O_5}$ is nonequivalent for $\mathrm{Mn^{3+}}$ ($\sim \pm 10^\circ$) and $\mathrm{Mn^{4+}}$ ($\sim \pm 14^\circ$) ions while it is the same between $\mathrm{Mn^{3+}}$ and $\mathrm{Mn^{4+}}$ ions in $\mathrm{BiMn_2O_5}$. Hence, it is possible that the rotated manner of the zigzag Mn chains running along *a* is disparate for $\mathrm{YMn_2O_5}$ and $\mathrm{BiMn_2O_5}$. Besides, the *c*-axis component of $\mathrm{Mn^{4+}}$ moments is extremely small in the $\mathrm{BiMn_2O_5}$ sample, indicating the weaker influence of P_{SC} to P_{tot}.

In the $H//b$ geometry, the scenario looks simple in comparison with the result of $H//a$, as shown in Fig. 5(b). Application of high magnetic fields contributes to a gradual suppression of the ICM2/FE2 phase and reentrance of the CM/FE1 phase. Meanwhile, the field-induced polarization reversal is observed again. It is worth mentioning that this region between the ICM2/FE2 and CM/FE1 phases below 10 K could originate from the two-phase coexistence of FE1 and FE2 leading to multidomain structures. This can be supported by a series of anomalies in the H-falling sweep, i.e., the motion of the domains [see Fig. 3(c)]. As expected, the number of these anomalies is severely dependent on different samples, as shown in Fig. S2 of the Supplemental Material [45]. Based on the classical mean-field theory, the lack of spin-flop transitions is normal in the case of $H//c$ on account of the hard axis. Furthermore, the magnetization increases linearly up to 54 T at low temperatures, indicating that the Mn spin slowly rotates towards collinearity due to strong exchange interactions. Correspondingly, a very broad peak that spans about 20 T is distinctly observed in dP_{b}/dH curves below 18 K (see Fig. S4 of the Supplemental Material [45]).

We note that the *b*-axis polarization of $\mathrm{YMn_2O_5}$ has been reported under magnetic fields [58]. Overall, the profile of $P_{\mathrm{b}}(H)$ curves measured by Kadomtseva *et al.* is roughly similar to our results within 25 T. However, several different features between us are clearly seen. First, no experimental data below 10 K or above 25 T are reported. Second, for $H//a$, there is not a large loop in the present work below 15 T and 25 K. Third, in the $H//b$ geometry, we do not see this anomaly above 18 K reported in Ref. [58]. Such discrepancy may be attributed to the limit of the measurement technology in the past. As is well known, the larger sweeping magnetic field dB/dt is more beneficial to the sensitivity of the polarization measurement. Our 10.5-ms short-pulse wave generated by a nondestructive magnet is a strong support for detecting the variation of $P(H)$ curves in $\mathrm{YMn_2O_5}$, which has been successfully applied in some multiferroics [2,44,53,57,59].

V. CONCLUSION

In conclusion, we have performed the high-field magnetization and ferroelectric polarization measurements to study the evolution of multiferroic properties of the single-crystal $\mathrm{YMn_2O_5}$ under the high magnetic field. Several magnetic phase transitions are clearly observed which are strongly dependent on the direction and strength of magnetic fields and temperatures. It indicates that the strong magnetic anisotropy can be undoubtedly identified in $\mathrm{YMn_2O_5}$. Correspondingly, pyroelectric measurements demonstrate distinct $P(H)$ curves along different crystallographic axes, suggesting a strong ME coupling. Particularly, a field-induced P reversal is realized for all directions of the magnetic field at low temperatures, which may be attributed to different origins. Based on the above experimental data, the high-field ME phase diagrams are constructed. It should be noted that the magnetization of $\mathrm{YMn_2O_5}$ is far from the saturation value even at the highest magnetic field. And, the higher magnetic field is desirable in order to obtain more interesting behaviors. Therefore, our experimental results lay a solid foundation for an overall understanding of the magnetic phase transitions and the ME coupling in rare-earth multiferroic manganites.

ACKNOWLEDGMENTS

This work was supported by the National Natural Science Foundation of China (Grants No. 12074135 and No. 12104351), Hubei Province Natural Science Foundation of China (Grants No. 2020CFA083 and No. 2021CFB027) and China Postdoctoral Science Foundation (Grant No. 2023M731209).

---

[1] L. Ponet, S. Artyukhin, T. Kain, J. Wettstein, A. Pimenov, A. Shuvaev, X. Wang, S.-W. Cheong, M. Mostovoy, and A. Pimenov, Topologically protected magnetoelectric switching in a multiferroic, Nature (London) **607**, 81 (2022).

[2] Y. T. Chang, Y. K. Weng, Y. L. Xie, B. You, J. F. Wang, L. Li, J.-M. Liu, S. Dong, and C. L. Lu, Colossal linear magnetoelectricity in polar magnet $Fe_2Mo_3O_8$, Phys. Rev. Lett. **131**, 136701 (2023).

[3] C. Lu, M. Wu, L. Lin, and J.-M. Liu, Single-phase multiferroics: new materials, phenomena, and physics, Natl. Sci. Rev. **6**, 653 (2019).

[4] S.-W. Cheong and M. Mostovoy, Multiferroics: a magnetic twist for ferroelectricity, Nat. Mater. **6**, 13 (2007).

[5] T. Weigel, C. Richter, M. Nentwich, E. Mehner, V. Garbe, L. Bouchenoire, D. Novikov, D. C. Meyer, and M. Zschornak, Picometer atomic displacements behind ferroelectricity in the commensurate low-temperature phase in multiferroic YMn_2O_5, Phys. Rev. B **109**, 054101 (2024).

[6] K. Zhai, D. S. Shang, Y. S. Chai, G. Li, J. W. Cai, B. G. Shen, and Y. Sun, Room-temperature nonvolatile memory based on a single-phase multiferroic hexaferrite, Adv. Funct. Mater. **28**, 1705771 (2018).

[7] N. Hur, S. Park, P. A. Sharma, J. Ahn, S. Guha, and S.-W. Cheong, Electric polarization reversal and memory in a multiferroic material induced by magnetic fields, Nature (London) (London) **429**, 392 (2004).

[8] T. Kimura, T. Goto, H. Shintani, K. Ishizaka, T. Arima, and Y. Tokura, Magnetic control of ferroelectric polarization, Nature (London) **426**, 55 (2003).

[9] N. Lee, C. Vecchini, Y. J. Choi, L. C. Chapon, A. Bombardi, P. G. Radaelli, and S.-W. Cheong, Giant tunability of ferroelectric polarization in $GdMn_2O_5$, Phys. Rev. Lett. **110**, 137203 (2013).

[10] T. Aoyama, K. Yamauchi, A. Iyama, S. Picozzi, K. Shimizu, and T. Kimura, Giant spin-driven ferroelectric polarization in $TbMnO_3$ under high pressure, Nat. Commun. **5**, 4927 (2014).

[11] T. Aoyama, A. Iyama, K. Shimizu, and T. Kimura, Multiferroicity in orthorhombic RMnO$_3$ (R = Dy, Tb, and Gd) under high pressure, Phys. Rev. B **91**, 081107(R) (2015).

[12] W. Peng, V. Balédent, C. V. Colin, T. C. Hansen, M. Greenblatt, and P. Foury-Leylekian, Tuning competing magnetic interactions with pressure in RMn$_2$O$_5$ multiferroics, Phys. Rev. B **99**, 245109 (2019).

[13] Y. Ishii, Y. Murakoshi, N. Sato, Y. Noda, T. Honda, H. Nakao, Y. Murakami, and H. Kimura, Isotropic magnetoelectric effect in $Tb_{1-x}Gd_xMn_2O_5$ studied by resonant x-ray scattering, Phys. Rev. B **100**, 104416 (2019).

[14] M. Tokunaga, Y. Yamasaki, Y. Onose, M. Mochizuki, N. Furukawa, and Y. Tokura, Novel multiferroic state of $Eu_{1-x}Y_xMnO_3$ in high magnetic fields, Phys. Rev. Lett. **103**, 187202 (2009).

[15] H. Wang, C. Li, S. Yuan, J. Wang, C. Lu, and J.-M. Liu, The crucial role of Mn spiral spin order in stabilizing the Dy-Mn exchange striction in multiferroic $DyMnO_3$, Phys. Chem. Chem. Phys. **19**, 3706 (2017).

[16] S. Partzsch, S. B. Wilkins, J. P. Hill, E. Schierle, E. Weschke, D. Souptel, B. Büchner, and J. Geck, Observation of electronic ferroelectric polarization in multiferroic YMn_2O_5, Phys. Rev. Lett. **107**, 057201 (2011).

[17] C. Wilkinson, P. J. Brown, and T. Chatterji, Temperature evolution of the magnetic structure of $TbMn_2O_5$, Phys. Rev. B **84**, 224422 (2011).

[18] Y. Noda, H. Kimura, M. Fukunaga, S. Kobayashi, I. Kagomiya, and K. Kohn, Magnetic and ferroelectric properties of multiferroic RMn$_2$O$_5$, J. Phys.: Condens. Matter **20**, 434206 (2008).

[19] C. Vecchini, L. Chapon, P. Brown, T. Chatterji, S. Park, S. Cheong, and P. Radaelli, Commensurate magnetic structures of RMn$_2$O$_5$ (R = Y, Ho, Bi) determined by single-crystal neutron diffraction, Phys. Rev. B **77**, 134434 (2008).

[20] G. R. Blake, L. C. Chapon, P. G. Radaelli, S. Park, N. Hur, S.-W. Cheong, and J. Rodriguez-Carvajal, Spin structure and magnetic frustration in multiferroic RMn$_2$O$_5$ (R = Tb, Ho, Dy), Phys. Rev. B **71**, 214402 (2005).

[21] C. R. dela Cruz, B. Lorenz, Y. Y. Sun, Y. Wang, S. Park, S.-W. Cheong, M. M. Gospodinov, and C. W. Chu, Pressure-induced enhancement of ferroelectricity in multiferroic RMn$_2$O$_5$ (R = Tb, Dy, Ho), Phys. Rev. B **76**, 174106 (2007).

[22] C. R. dela Cruz, F. Yen, B. Lorenz, M. M. Gospodinov, C.-W. Chu, W. Ratcliff, J. W. Lynn, S. Park, and S.-W. Cheong, Structural anomalies at the magnetic and ferroelectric transitions in RMn$_2$O$_5$ (R = Tb, Dy, Ho), Phys. Rev. B **73**, 100406(R) (2006).

[23] D. P. Kozlenko, N. T. Dang, S. E. Kichanov, E. V. Lukin, A. M. Pashayev, A. I. Mammadov, S. H. Jabarov, L. S. Dubrovinsky, H.-P. Liermann, W. Morgenroth, R. Z. Mehdiyeva, V. G. Smotrako, and B. N. Savenko, Competing magnetic and structural states in multiferroic YMn_2O_5 at high pressure, Phys. Rev. B **92**, 134409 (2015).

[24] S. Dong, H. Xiang, and E. Dagotto, Magnetoelectricity in multiferroics: a theoretical perspective, Natl. Sci. Rev. **6**, 629 (2019).

[25] Y. Tokura, S. Seki, and N. Nagaosa, Multiferroics of spin origin, Rep. Prog. Phys. **77**, 076501 (2014).

[26] H. Kimura, Y. Sakamoto, M. Fukunaga, H. Hiraka, and Y. Noda, Control of magnetic interaction and ferroelectricity by nonmagnetic Ga substitution in multiferroic YMn_2O_5, Phys. Rev. B **87**, 104414 (2013).

[27] S. Wakimoto, H. Kimura, Y. Sakamoto, M. Fukunaga, Y. Noda, M. Takeda, and K. Kakurai, Role of magnetic chirality in polarization flip upon a commensurate-incommensurate magnetic phase transition in YMn_2O_5, Phys. Rev. B **88**, 140403(R) (2013).

[28] R. P. Chaudhury, C. R. Dela Cruz, B. Lorenz, Y. Sun, C.-W. Chu, S. Park, and S.-W. Cheong, Pressure-induced polarization reversal in multiferroic YMn_2O_5, Phys. Rev. B **77**, 220104(R) (2008).

[29] F. Wunderlich, T. Leisegang, T. Weißbach, M. Zschornak, H. Stöcker, J. Dshemuchadse, A. Lubk, T. Führlich, E. Welter, D. Souptel, S. Gemming, G. Seifert, and D. C. Meyer, EXAFS, XANES, and DFT study of the mixed-valence compound $\mathrm{YMn_2O_5}$: Site-selective substitution of Fe for Mn, Phys. Rev. B **82**, 014409 (2010).

[30] M. Deutsch, T. C. Hansen, M. T. Fernandez-Diaz, A. Forget, D. Colson, F. Porcher, and I. Mirebeau, Pressure-induced commensurate phase with potential giant polarization in $\mathrm{YMn_2O_5}$, Phys. Rev. B **92**, 060410(R) (2015).

[31] A. Munoz, J. Alonso, M. Martínez-Lope, and J. Martínez, Synthesis, structural, and magnetic characterization of a new ferrimagnetic oxide: $\mathrm{YFeMnO_5}$, Chem. Mater. **16**, 4087 (2004).

[32] T.-C. Han and J. G. Lin, Enhancement of magnetic moment in Ca-doped helimagnetic $\mathrm{YMn_2O_5}$, J. Magn. Magn. Mater. **304**, e424 (2006).

[33] J.-H. Kim, S.-H. Lee, S. Park, M. Kenzelmann, A. B. Harris, J. Schefer, J.-H. Chung, C. F. Majkrzak, M. Takeda, and S. Wakimoto, Spiral spin structures and origin of the magnetoelectric coupling in $\mathrm{YMn_2O_5}$, Phys. Rev. B **78**, 245115 (2008).

[34] M. Fukunaga, Y. Sakamoto, H. Kimura, Y. Noda, N. Abe, K. Taniguchi, T. Arima, S. Wakimoto, M. Takeda, K. Kakurai, and K. Kohn, Magnetic-field-induced polarization flop in multiferroic $\mathrm{TmMn_2O_5}$, Phys. Rev. Lett. **103**, 077204 (2009).

[35] M. Fukunaga, Y. Sakamoto, H. Kimura, and Y. Noda, Magnetic phase transitions and magnetic-field-induced polarization flops in multiferroic $\mathrm{YbMn_2O_5}$, J. Phys. Soc. Jpn. **80**, 014705 (2010).

[36] T. Goto, T. Kimura, G. Lawes, A. Ramirez, and Y. Tokura, Ferroelectricity and giant magnetocapacitance in perovskite rare-earth manganites, Phys. Rev. Lett. **92**, 257201 (2004).

[37] B. M. Wanklyn, Flux growth of some complex oxide materials, J. Mater. Sci. **7**, 813 (1972).

[38] M. Tachibana, K. Akiyama, H. Kawaji, and T. Atake, Lattice effects in multiferroic $R\mathrm{Mn_2O_5}$ (R = Sm-Dy, Y), Phys. Rev. B **72**, 224425 (2005).

[39] L. Chapon, P. G. Radaelli, G. R. Blake, S. Park, and S.-W. Cheong, Ferroelectricity induced by acentric spin-density waves in $\mathrm{YMn_2O_5}$, Phys. Rev. Lett. **96**, 097601 (2006).

[40] S. Kobayashi, T. Osawa, H. Kimura, Y. Noda, I. Kagomiya, and K. Kohn, Reinvestigation of simultaneous magnetic and ferroelectric phase transitions in $\mathrm{YMn_2O_5}$, J. Phys. Soc. Jpn. **73**, 1593 (2004).

[41] D. Higashiyama, S. Miyasaka, and Y. Tokura, Magnetic-field-induced polarization and depolarization in $\mathrm{HoMn_2O_5}$ and $\mathrm{ErMn_2O_5}$, Phys. Rev. B **72**, 064421 (2005).

[42] D. Higashiyama, S. Miyasaka, N. Kida, T. Arima, and Y. Tokura, Control of the ferroelectric properties of $\mathrm{DyMn_2O_5}$ by magnetic fields, Phys. Rev. B **70**, 174405 (2004).

[43] J. W. Kim, S. Haam, Y. S. Oh, S. Park, S.-W. Cheong, P. Sharma, M. Jaime, N. Harrison, J. H. Han, G.-S. Jeon, P. Coleman, and K. H. Kim, Observation of a multiferroic critical end point, Proc. Natl. Acad. Sci. USA **106**, 15573 (2009).

[44] T. Li, H. W. Wang, Y. R. Song, C. Dong, R. Chen, M. Yang, and J. F. Wang, Doping-controlled quantum magnetization plateau and high-field ferroelectricity in multiferroic $\mathrm{Ni_{2-\mathit{x}}T_\mathit{x}V_2O_7}$ (T = Zn or Mn), Phys. Rev. B **108**, 224414 (2023).

[45] See Supplemental Material at http://link.aps.org/supplemental/10.1103/PhysRevB.110.014430 for more experimental results: the bond angle and bond length of $\mathrm{YMn_2O_5}$ and $\mathrm{BiMn_2O_5}$; measured magnetization as a function of H at 1.6 K under the higher magnetic field; ΔP_b as a function of $H//b$ with sample No. 2 measured at various temperatures; the temperature dependence of the magnetic susceptibility χ along three crystallographic axes at various magnetic fields; the derivative dP_b/dH as a function of H measured at various temperatures for $H//c$, which includes Ref. [46].

[46] A. Munoz, J. A. Alonso, M. T. Casais, M. J. Martínez-Lope, J. L. Martínez, and M. T. Fernández-Díaz, Magnetic structure and properties of $\mathrm{BiMn_2O_5}$ oxide: A neutron diffraction study, Phys. Rev. B **65**, 144423 (2002).

[47] R. D. Shannon, Revised effective ionic radii and systematic studies of interatomic distances in halides and chalcogenides, Acta Crystallogr., Sect. A **32**, 751 (1976).

[48] G. S. Jeon, J.-H. Park, J. W. Kim, K. H. Kim, and J. H. Han, Theory of magnetic-field-induced critical end point in $\mathrm{BiMn_2O_5}$, Phys. Rev. B **79**, 104437 (2009).

[49] S. Baidya, P. Sanyal, H. Das, B. Roessli, T. Chatterji, and T. Saha-Dasgupta, Understanding neutron scattering data in $\mathrm{YMn_2O_5}$: An effective spin Hamiltonian, Phys. Rev. B **84**, 054444 (2011).

[50] S. Bukhari, T. Kain, M. Schiebl, A. Shuvaev, A. Pimenov, A. Kuzmenko, X. Wang, S.-W. Cheong, J. Ahmad, and A. Pimenov, Magnetoelectric phase diagrams of multiferroic $\mathrm{GdMn_2O_5}$, Phys. Rev. B **94**, 174446 (2016).

[51] V. Balédent, A. Vaunat, S. Petit, L. Nataf, S. Chattopadhyay, S. Raymond, and P. Foury-Leylekian, Electronic ground-state hysteresis under magnetic field in $\mathrm{GdMn_2O_5}$, Phys. Rev. B **108**, 104419 (2023).

[52] S. Chattopadhyay, V. Balédent, S. Panda, S. Yamamoto, F. Duc, T. Herrmannsdörfer, M. Uhlarz, T. Gottschall, O. Mathon, Z. Wang, C. Strohm, M. Greenblatt, P. Foury-Leylekian, and J. Wosnitza, $4f$ spin driven ferroelectric-ferromagnetic multiferroicity in $\mathrm{PrMn_2O_5}$ under a magnetic field, Phys. Rev. B **102**, 094408 (2020).

[53] J. F. Wang, W. X. Liu, Z. Z. He, C. B. Liu, M. Tokunaga, M. Li, C. Dong, X. T. Han, F. Herlach, C. L. Lu, Z. W. Ouyang, Z. C. Xia, K. Kindo, L. Li, and M. Yang, Ferroelectric polarization reversal in multiferroic $\mathrm{MnWO_4}$ via a rotating magnetic field up to 52 T, Phys. Rev. B **104**, 014415 (2021).

[54] H. Kimura, K. Nishihata, Y. Noda, N. Aso, K. Matsubayashi, Y. Uwatoko, and T. Fujiwara, Pressure-induced commensurate magnetic order in multiferroic $\mathrm{HoMn_2O_5}$, J. Phys. Soc. Jpn. **77**, 063704 (2008).

[55] H. Kimura, Y. Kamada, Y. Noda, K. Kaneko, N. Metoki, and K. Kohn, Ferroelectricity induced by incommensurate-commensurate magnetic phase transition in multiferroic $\mathrm{HoMn_2O_5}$, J. Phys. Soc. Jpn. **75**, 113701 (2006).

[56] S. Kobayashi, T. Osawa, H. Kimura, Y. Noda, I. Kagomiya, and K. Kohn, 2D-to-1D modulated-to-lock in successive magnetic phase transitions associated with ferroelectricity in $\mathrm{ErMn_2O_5}$, J. Phys. Soc. Jpn. **73**, 1031 (2004).

[57] R. Chen, J. F. Wang, Z. W. Ouyang, M. Tokunaga, A. Y. Luo, L. Lin, J. M. Liu, Y. Xiao, A. Miyake, Y. Kohama, C. L. Lu, M. Yang, Z. C. Xia, K. Kindo, and L. Li, Successive electric-polarization switches in the $S = 1/2$ skew chain $Co_2V_2O_7$ induced by a high magnetic field, Phys. Rev. B **100**, 140403(R) (2019).

[58] A. M. Kadomtseva, Y. F. Popov, G. P. Vorob'ev, K. I. Kamilov, P. N. Makhov, M. M. Tehranchi, and A. Phirouznia, Induced by magnetic field spin reorientation in YMn_2O_5, Physica B **329**, 856 (2003).

[59] J. H. Zhang, L. Lin, C. Dong, Y. T. Chang, J. F. Wang, C. L. Lu, P. Z. Chen, W. J. Zhai, G. Z. Zhou, L. Huang, Y. S. Tang, S. H. Zheng, M. F. Liu, X. H. Zhou, Z. B. Yan, and J.-M. Liu, High-field magnetoelectric coupling and successive magnetic transitions in the Mn-doped polar antiferromagnet Ni_3TeO_6, Phys. Rev. B **109**, 184112 (2024).